The effect of particle design on cellular internalization pathways

Stephanie E. A. Gratton*, Patricia A. Ropp*, Patrick D. Pohlhaus*, J. Christopher Luft*, Victoria J. Madden†, Mary E. Napier*, and Joseph M. DeSimone†‡§¶

Departments of *Chemistry and Carolina Center of Cancer Nanotechnology Excellence, †Pathology, and ‡Pharmacology and Lineberger Comprehensive Cancer Center, University of North Carolina, Chapel Hill, NC 27599; and §Department of Chemical and Biomolecular Engineering, North Carolina State University, Raleigh, NC 27695

Edited by Mark E. Davis, California Institute of Technology, Pasadena, CA, and approved June 6, 2008 (received for review February 22, 2008)

The interaction of particles with cells is known to be strongly influenced by particle size, but little is known about the interdependent role that size, shape, and surface chemistry have on cellular internalization and intracellular trafficking. We report on the internalization of specially designed, monodisperse hydrogel particles into HeLa cells as a function of size, shape, and surface charge. We employ a top-down particle fabrication technique called PRINT that is able to generate uniform populations of organic micro- and nanoparticles with complete control of size, shape, and surface chemistry. Evidence of particle internalization was obtained by using conventional biological techniques and transmission electron microscopy. These findings suggest that HeLa cells readily internalize nonspherical particles with dimensions as large as 3 μm by using several different mechanisms of endocytosis. Moreover, it was found that rod-like particles enjoy an appreciable advantage when it comes to internalization rates, reminiscent of the advantage that many rod-like bacteria have for internalization in nonphagocytic cells.

PRINT | shape | size | surface charge

Definitive biodistribution maps that establish the interdependency of the size, shape, and surface chemistry of nanoparticles *in vitro* and *in vivo* over length scales ranging from cells to tissues to the entire organism are needed by many different research communities. Environmental regulators, pulmonologists, oncologists, pharmaceutical scientists, toxicologists, cell biologists, and dermatologists all need definitive answers related to particle biodistribution, particle permeability, and transport by using "calibration quality" particles. For example, fungal and bacterial pathogens are first and foremost recognized by their form or shape; however, the complete understanding of the role and significance of that form and shape is largely lacking. Indeed, some rod-like bacterial pathogens, including the Gram-negative bacteria *Salmonella*, *Shigella*, and *Yersinia* and the Gram-positive bacterium *Listeria monocytogenes* can induce their entry into nonphagocytic mammalian cells (1). As such, nanofabricated tools (e.g., precisely defined particles) hold significant promise to provide insight into the fundamentals of cellular and biological processes. These tools can also yield essential insights into the design of effective vectors for use in nanomedicine, especially for the design of nanoparticles for use as targeted therapeutics and imaging agents. Indeed, very little is known how the interdependency of size, shape, and surface chemistry can influence the biodistribution, cellular internalization, and intracellular trafficking of micro- and nanoparticles. The most prominent approaches for synthesizing nanoparticles have involved "bottom-up" chemical processes including the self-assembly of molecules [e.g., liposomes (2), micelles (3), and polyplexes (4)], the synthesis of macromolecules [e.g., microemulsions (5), dendrimers (6), immunoconjugates (7)], or the synthesis of carbon nanotubes (8) and inorganic particles (9). Such bottom-up approaches have significant limitations with regard to the systematic study of key particle variables on biological processes (10, 11), such as size, shape, chemical composition, and surface charge (12–14).

Understanding the interactions of precisely defined particles with cells forms the basis on which fundamental *in vitro*, and *in vivo* studies can build. Calibration quality particles can also be used to screen for potential environmental hazards. Several reports have addressed the role of shape and size on cellular internalization (12, 15); however, no particle fabrication techniques currently available have the ability to independently alter one variable at a time, and monitor the effect of each variable. We have focused on extending emerging "top-down" fabrication techniques (16) from the microelectronics industry for the facile synthesis of readily tailorable nanofabricated tools or particles (11, 17) that can allow for the attainment of detailed knowledge of the interdependent effect that key particle variables (such as size, shape, chemical composition, and surface charge) have on cellular entry.

Results and Discussion

We designed a series of particles with varying sizes and shapes at a constant chemical composition (i.e., at a constant surface charge) by using a top-down lithographic fabrication method called PRINT (*P*article *R*eplication *I*n *N*on-wetting *T*emplates) (17–19). The PRINT micro- and nanoparticles were made from cationic, cross-linked poly(ethylene glycol) hydrogels and were designed to study the interdependent effect of size, shape, and surface charge (zeta potential) on their internalization by human cervical carcinoma epithelial (HeLa) cells. Three distinct series of cationic poly(ethylene glycol)-based particles were fabricated: a micrometer-sized series of cubic-shaped particles (cube side length = 2 μm, 3 μm, and 5 μm; Fig. 1 *A–F*); a micrometer-sized cylindrical series with identical heights but varying diameters [diameter = 0.5 μm, aspect ratio (AR) = 2 (Fig. 1*G*); or diameter = 1 μm, AR = 1 (Fig. 1*H*)]; and finally, a cylindrical-shaped nanoparticle series [diameter = 200 nm, AR = 1 (Fig. 1*I*), diameter = 100 nm, AR = 3 (Fig. 1*J*); diameter = 150 nm, AR = 3 (Fig. 1*K*)].

The cellular internalization of the three sets of particles was examined by using HeLa cells, with particles being dosed at a constant particle mass (15 μg/ml). The kinetics of particle internalization was evaluated by using a flow cytometry method

Author contributions: S.E.A.G., P.A.R., P.D.P., J.C.L., V.J.M., M.E.N., and J.M.D. designed research; S.E.A.G., P.A.R., P.D.P., J.C.L., and V.J.M. performed research; S.E.A.G., P.A.R., P.D.P., J.C.L., V.J.M., M.E.N., and J.M.D. analyzed data; and S.E.A.G., P.A.R., M.E.N., and J.M.D. wrote the paper.

Conflict of interest statement: The research reported in this paper received partial financial support from a venture capital-backed company that Dr. Joseph M. DeSimone cofounded, Liquidia Technologies (www.liquidia.com). Currently he is on the board of directors and has personal financial interests in Liquidia Technologies.

This article is a PNAS Direct Submission.

¶To whom correspondence should be addressed. E-mail: desimone@unc.edu.

This article contains supporting information online at www.pnas.org/cgi/content/full/0801763105/DCSupplemental.

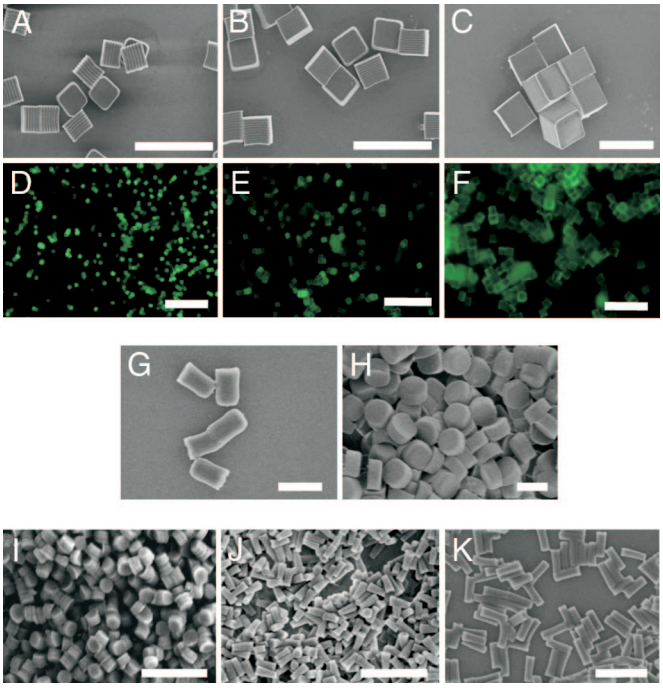

Fig. 1. Micrographs of PRINT particles varying in both size and shape. The particle composition for these experiments was 67 wt % trimethyloylpropane ethoxylate triacrylate (MW = 428 g/mol), 20 wt % poly(ethylene glycol) monomethylether monomethacrylate (MW = 1,000 g/mol), 10 wt % 2-aminoethylmethacrylate hydrochloride (AEM·HCl), 2 wt % fluorescein-*O*-acrylate, and 1 wt % 2,2-diethoxyacetophenone. (*A–C*) Scanning electron micrograph of the cubic series of particles [diameters equal to 2 μm (*A*), 3 μm (*B*), and 5 μm (*C*)]. (*D–F*) Fluorescence micrographs of the cubic series of particles [diameters equal to 2 μm (*D*), 3 μm (*E*), and 5 μm (*F*)]. (*G* and *H*) Scanning electron micrographs of the cylindrical series of microparticles having the same height (1 μm), but varying diameters [diameter = 0.5 μm (*G*) and 1 μm (*H*)]. (*I–K*) Scanning electron micrographs of the series of cylindrical nanoparticles [diameter = 200 nm, height = 200 nm (*I*); diameter = 100 nm, height = 300 nm (*J*); diameter = 150 nm, height = 450 nm (*K*)]. (Scale bars: *A–F*, 20 μm; *G–K*, 1 μm.)

in which internalized particles were differentiated from membrane-bound particles with a trypan blue fluorescence quench (20). The time course of particle internalization was studied from 15 min to 4 h (Fig. 2). Cellular internalization of PRINT particles exhibited a strong dependence on particle size and shape. No significant internalization of the cubic particles with side lengths of 3 and 5 μm was seen in contrast to cubic particles with a side length of 2 μm that were significantly internalized by a large fraction of the cells. Cylindrical particles having diameters equal to 500 nm and 1 μm, both having heights of 1 μm, displayed similar internalization profiles, internalizing particles at a higher percentage (≈75%) than cubic-shaped 2-μm particles (≈45%).

It was found that HeLa cells internalized all three nanoparticle shapes in the cylindrical series to a very high degree, but the kinetics of internalization were quite varied among the members of this series. Although the low-aspect-ratio cylindrical particles having a diameter = 200 nm and a height = 200 nm and the high-aspect-ratio cylindrical particles having a diameter = 150 nm and a height = 450 nm have similar volumes (6.3×10^{-3} μm^3 and 7.9×10^{-3} μm^3, respectively), their rates of internalization were quite different. The high-aspect-ratio particles (d = 150 nm, h = 450 nm) were internalized by HeLa cells ≈4 times faster than the more symmetric low-aspect-ratio particles (d = 200 nm, h = 200 nm) (5.2% of the cell population per min vs. 1.2% of the cell population per min). Cylindrical particles having a diameter of 100 nm, an aspect ratio of 3, and a volume of 2.4×10^{-3} μm^3 were internalized to a lesser extent than the larger cylindrical

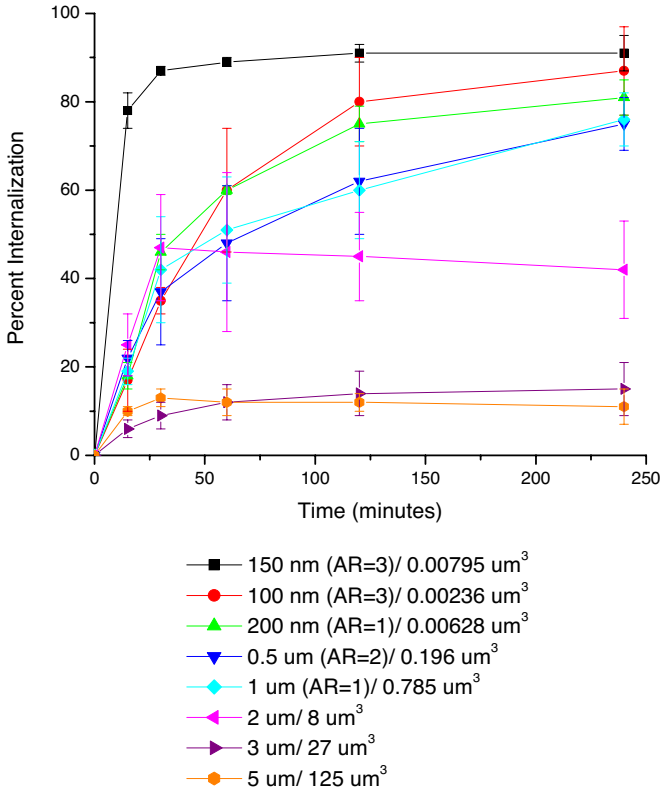

Fig. 2. Internalization profile of PRINT particles with HeLa cells over a 4-h incubation period at 37°C. Legend depicts the particle diameter per particle volume.

particles having a diameter of 150 nm with the same aspect ratio. The internalization kinetics of the nanoparticles by HeLa cells thus appears to depend not only on the effective rod-like character (aspect ratio), but also on the absolute size and/or volume of the particle. A possible explanation for this behavior could be attributed to the multivalent cationic interactions with cells that are available with the higher-aspect-ratio particles because of the larger surface areas in contact with the cell membrane.

High molecular weight, positively charged polyelectrolytes such as poly(lysine) are known to exhibit cytotoxicity *in vitro* because of interactions between the polyelectrolytes and cell membrane phospholipids resulting in disruption of the cellular

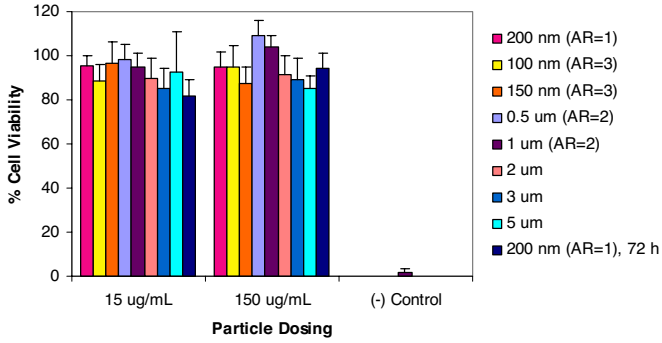

Fig. 3. MTS assay showing the cytotoxicity of all particles under investigation. All experiments were carried out with a 4-h incubation with HeLa cells, except the final bar, where the 200-nm particles were tested for cytotoxicity to 72 h.

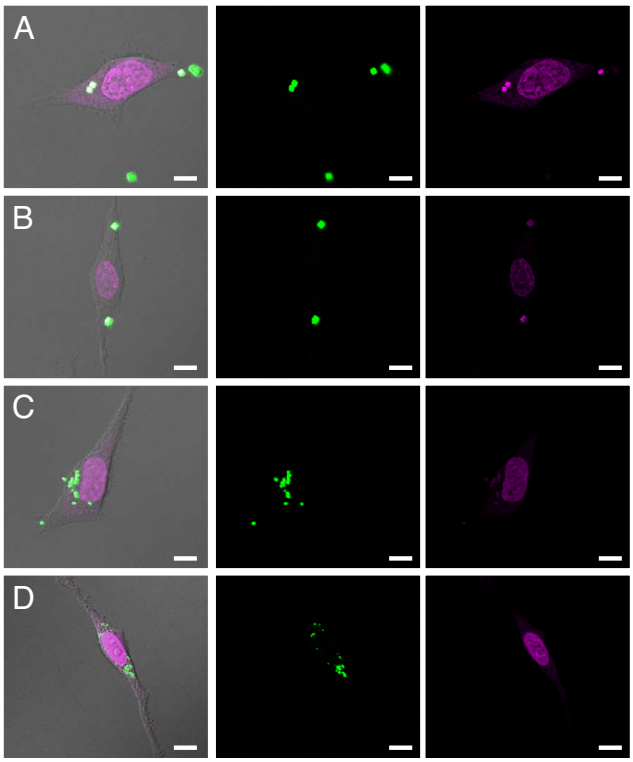

Fig. 4. Confocal laser scanning microscopy images of HeLa cells after a 1-h incubation period at 37°C with 3-μm cubes (*A*), 2-μm cubes (*B*), 1-μm (AR = 1) cylinders (*C*), and 200-nm (AR = 1) cylindrical particles (*D*). (scale bar: 10 μm.)

membrane structure (21, 22). Therefore, the cytotoxicity of each particle series was determined by using the 3-(4,5-carboxymethoxyphenyl)-2-(4-sulfophenyl)-2H-tetrazolium (MTS) cell viability assay (Fig. 3). No toxicity was evident from the assays suggesting that cationic PRINT particles used in this study were nontoxic at the concentration ranges used herein. Furthermore, because nanoparticles are likely candidates for *in vivo* studies (20), we evaluated the low-aspect-ratio cylindrical particles (d = 200 nm, h = 200 nm) for long-term cytotoxic effects (72 h) (Fig. 3). Even under extended incubation times, PRINT nanoparticles exhibited no cytotoxicity.

Numerous studies have shown that surface charge has a significant impact on cellular internalization of a variety of nanocarriers (23). Dependence of surface charge on cellular internalization of PRINT nanoparticles was investigated by using rapidly internalized high-aspect-ratio cylindrical nanoparticles (d = 150 nm, h = 450 nm). These particles were treated with acetic anhydride to passivate the surface amine groups, thereby changing the zeta potential from +34.8 ± 3.0 mV to −33.7 ± 2.3 mV on conversion of the protonated surface amine groups to amides (supporting information (SI) Figs. S1–S13 and Tables S1 and S2). The charge effect on cellular internalization was dramatic. Positively charged nanoparticles were internalized in 84% of cells after a 1-h incubation period, whereas the identically shaped, negatively charged particles were not internalized to any significant amount (<5%), thus, strongly suggesting that surface charge plays an important role in the cellular internalization of PRINT particles (Fig. S1).

Further insight into the cellular internalization of the cationic hydrogel particles was gained by confocal microscopy (Fig. 4, Fig. S2). Monitoring particle internalization by confocal microscopy gave a more complete understanding of particle intracellular localization. Confocal micrographs revealed that all internalized PRINT particles consistently migrated to the perinuclear region of the cells over time. Z series images were obtained and used to construct 3D representations that clearly show that PRINT particles as large as 3 μm are internalized by HeLa cells, and that the particles ultimately translocate to the perinuclear region of the cell. These data are consistent with intracellular translocation of either endosomal and/or lysosomal vesicles from the plasma membrane along microtubules in the minus direction toward the centrosome/microtubule-organizing center of the cell (24).

Transmission electron microscopy (TEM) was used to gain additional understanding of the mechanism of PRINT particle internalization by HeLa cells (Fig. 5 see also Figs. S3–S13). Cylindrical PRINT particles having a diameter of 200 nm (AR = 1) were readily internalized by HeLa cells through multiple modes of nonspecific endocytosis (Fig. 5 *B–D*). TEM micrographs of the low-aspect-ratio cylindrical particles (d = 200 nm, h = 200 nm) clearly show that the internalization of these particles occurs and that internalization is by a combination of mechanisms, most notably energy-dependent phagocytosis and a clathrin-mediated mechanism. At early times both mechanisms are observed. A clathrin-coated pit is clearly associated with an internalized particle, as seen in Fig. 5 *B* and *C*. Internalization at the surface is associated with actin rearrangement near the plasma membrane and extension into the extracellular space (Fig. 5*B*; see also Fig. S3). Furthermore, high-aspect-ratio nanoparticles (d = 150 nm, h = 450 nm) were rapidly internalized into HeLa cells and translocated close to the nuclear membrane (Fig. 5 *E* and *F*). At 1 h, these rod-like particles had traversed significantly further into the cells compared with both the low-aspect-ratio cylindrical nanoparticles (d = 200 nm, h = 200 nm) and the 1-μm (AR = 1) cylindrical particles at similar times. This observation qualitatively supports the rate data obtained by using flow cytometry. Fig. 5 *G–I* clearly shows the internalization and translocation of cylindrical 1-μm (AR = 1) PRINT particles deep within the cell over the time frame examined.

To more clearly delineate the role of specific endocytotic pathways involved in PRINT particle cellular internalization, HeLa cells were treated with known biochemical inhibitors of energy-dependent processes, clathrin-mediated endocytosis, caveolae-mediated endocytosis, and macropinocytosis (Fig. 6). To investigate energy dependence, cells were preincubated in the presence of NaN_3/2-deoxyglucose (NaN_3/DOG) and then treated with PRINT particles. NaN_3/DOG, which blocks cellular ATP synthesis, resulted in a marked decrease in the cellular internalization of all particle sizes (68–84% compared with nontreated cells) indicating that internalization is an energy-dependent process, with the smaller PRINT particles showing a slightly higher tendency for energy dependence [78% for 200-nm (AR = 1) and 84% for 150-nm (AR = 3) compared with the 68% for the larger 1-μm (AR = 1) particles]. Complete inhibition was not seen and is most likely because of the presence of exogenous ATP and glucose in the serum-free media. Similarly, internalization of the smaller PRINT particles was markedly decreased in the presence of cytochalasin D (63% and 77% for 200-nm and 150-nm particles, respectively), an inhibitor of actin polymerization as compared with the larger 1-μm particles (24%). Although cytochalasin D is generally classified as an inhibitor of macropinicytosis/phagocytosis, both clathrin- and caveolae-mediated pathways have recently been shown to require actin for formation and invagination of both coated pits and caveosomes (25). Because HeLa cells are considered as nonphagocytosing cells, the inhibition of particle internalization by cytochalasin D may reflect inhibition of either clathrin-mediated or caveolae-mediated pathways, or a combination of the two. Indeed, comparison of the cytochalasin inhibition with the inhibition of clathrin-mediated endocytosis by using the dynamin-GTPase inhibitor Dynasore (26) and inhibition of caveolae-mediated endocytosis with the natural isoflavone tyrosine kinase inhibitor

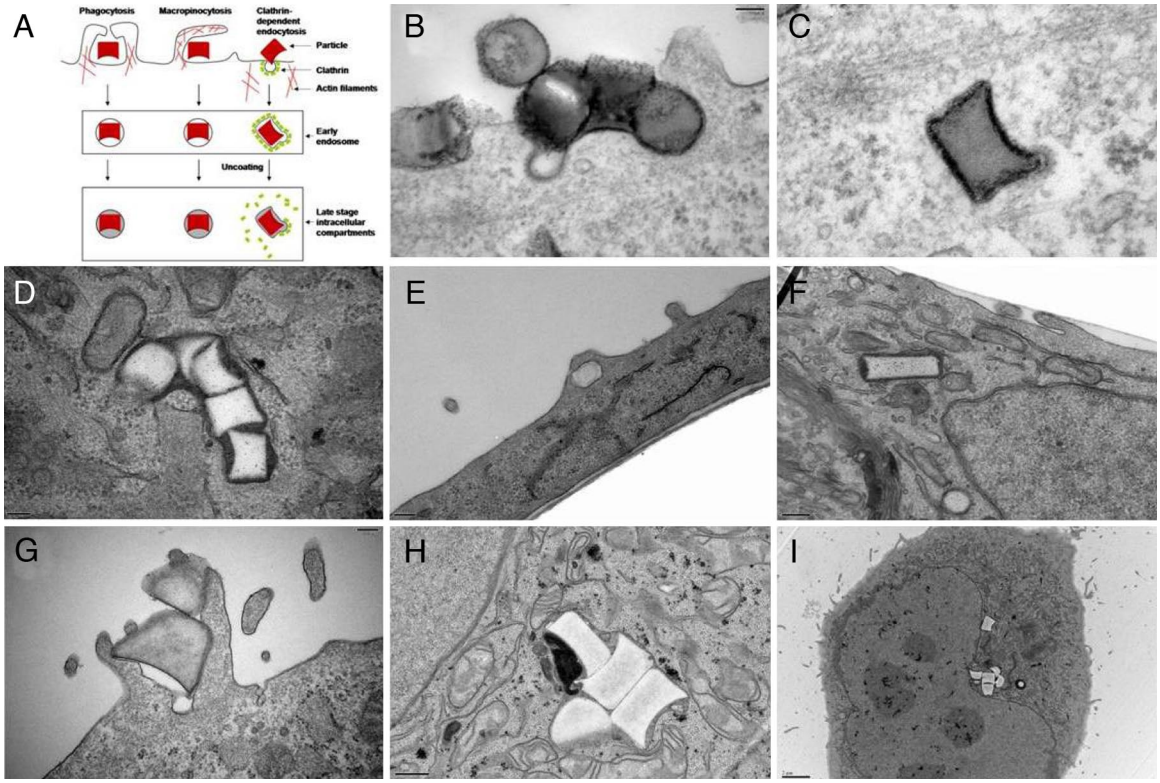

Fig. 5. Transmission electron microscopy images of HeLa cells at 37°C (incubation times in parentheses). (*A*) Illustration depicting the major pathways of cellular internalization used by PRINT particles. (*B–D*) With 200 nm (AR = 1) cylindrical particles (AR = 1) (*B* and *C*, 15 min; *D*, 4 h). (*E* and *F*) With 150 nm (AR = 3) cylindrical particles (*E* and *F*, 1 h). (*G–I*) With 1-μm (AR = 1) cylindrical particles (*G*, 1 h; *H* and *I*, 4 h).

genistein shows an almost identical inhibition pattern. The importance of actin involvement is also demonstrated in TEMs of all three sizes of particles (Fig. 5; see also Figs. S3–S13). Surprisingly, chlorpromazine, a cationic amphipathic drug also used to probe clathrin-mediated endocytosis, showed significant inhibition when compared with internalization in the presence of Dynasore with the 200-nm (AR = 1) and 1-μm (AR = 1) particle sizes being inhibited by 92% compared with ≈60% and 87% compared with ≈36%, respectively. No change was observed between the two inhibitors for the 150-nm (AR = 3) particles. Because of the amphipathic nature of the drug, chlorpromazine is readily capable of incorporating into the lipid bilayer of the plasma membrane increasing lipid fluidity, which in turn may inhibit or block the formation of membrane invaginations, thus leading to a decrease in particle internalization. Nonetheless, both chlorpromazine and Dynasore demonstrated the importance of the clathrin-mediated pathway for the internalization of the 150-nm (AR = 3) and 200-nm (AR = 1) cylindrical PRINT particles, where ≈70% inhibition of internalization was seen for the 150 nm (AR = 3) particles, and ≈60% inhibition was seen for the 200-nm (AR = 1) particles. The exact role of this pathway in the internalization of 1-μm (AR = 1) cylindrical PRINT particles is not clearly delineated because only ≈35% of internalization was inhibited in the presence of Dynasore, but >85% was observed with chlorpromazine. To discern any role that caveolae-mediated endcytosis may play in nanoparticle uptake, two inhibitors, genistein, a tyrosine kinase inhibitor, and methyl-β-cyclodextrin, a cyclic heptasaccharide known to sequester and alter cholesterol-rich domains within the plasma membrane, were used. For both inhibitors, caveolae-mediated endocytosis was observed to be a prominent internalization pathway for the 150-nm (AR = 3) and 200-nm (AR = 1) cylindrical PRINT particles (≈60% inhibition seen with both particles with both inhibitors) with very little inhibition detected with the larger 1-μm (AR = 1) PRINT particles (≈10–25%). These data are consistent with the current view that caveolae generally can only endocytose nanoparticles in the range of 50–100 nm (27). All of these experiments strongly suggest that clathrin-mediated and caveolae-mediated endocytosis and, to a much lesser extent,

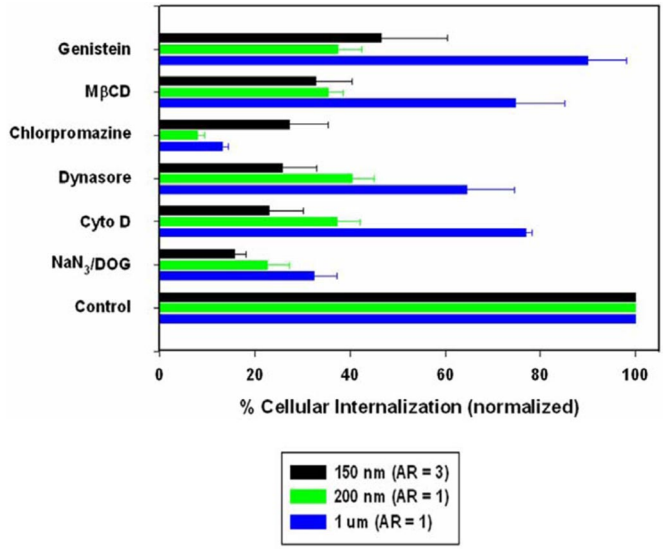

Fig. 6. Probing the mechanisms of cellular internalization by using inhibitors of endocytosis. HeLa cells were incubated with the indicated inhibitors in the graph as outlined in the experimental methods. Percent internalization was normalized to particle internalization in the absence of inhibitors.

macropinocytosis are involved with both the nano- and microparticle internalization, but these mechanisms play a larger role with the internalization of the smaller [150-nm (AR = 3) and the 200-nm (AR = 1)] PRINT nanoparticles. Note that none of the specific chemical inhibitors led to >95% inhibition of internalization. This observation most likely indicates the role of nonclathrin-, non-caveolae-mediated pathways for internalization. Interestingly, the rapidly internalizing 150-nm (AR = 3) particles use all internalization pathways to a large extent, possibly pointing to the reason why these particles are internalized to such a high degree relative to the other shapes.

The biochemical inhibitory studies, the confocal microscopy data, the TEM data, and the flow cytometry analysis of the precisely defined and shaped PRINT particles reveal a number of interesting results and a couple of surprises. First, current scientific thought is that the upper limit of the size of any nanoparticle internalized into nonphagocytotic cells by means of nonspecific endocytosis is 150 nm; thus, any particle >150 nm would be excluded from cellular internalization altogether (28–30). Our results suggest that this upper-size-limit convention needs to be raised significantly as we clearly see the internalization of 3-μm, 2-μm, and 1-μm particles. Second, our data reveal that internalized PRINT particles of any size appear to follow multiple pathways into the cell. Third, there was a significant diminution of particle internalization in cells when the particles had a negative zeta potential versus particles that had a positive zeta potential. The dramatic switch in the internalization of particles with the sign of the zeta potential points to a potential strategy for enhancing the specificity of particle targeting to cells of interest. It will be interesting to conjugate ligands capable of stimulating specific receptor-mediated endocytosis to particles having a negative zeta potential as a strategy to enhance the specificity of cell-targeting objectives. Fourth, it was surprising to find that the internalization of the rod-like, high-aspect-ratio nanoparticles (d = 150 nm, h = 450 nm) occurs much more rapidly and efficiently than would be expected based on size considerations alone, suggesting a special role associated with the shape of the particles. Specifically, these high-aspect-ratio, rod-like PRINT particles were internalized faster than their more symmetric 200-nm (AR = 1) cylindrical particle counterpart, even though both particles are substantially equal in volume. Furthermore, rod-like nanoparticles having the same aspect ratio and smaller dimensions (cylindrical particles with d = 100 nm and h = 300 nm vs. cylindrical particles with d = 150 nm and h = 450 nm) did not increase the amount of particles internalized into HeLa cells. Thus, the interplay between particle shape and size at constant surface chemistry will undoubtedly play a role in numerous areas of interest including particle-targeting strategies in therapeutic applications, environmental fate of nanoparticles, and the investigation of the rationale behind bacterial pathogen sizes and shapes.

Materials and Methods

PRINT Particle Preparation. In brief, 15 ml of Fluorocur resin (Liquidia Technologies) containing 0.1% (wt/wt) of 2,2-diethoxyacetophenone was poured onto the silicon master template inside an enclosed UV chamber. The chamber was degassed with nitrogen for 2 min, then the coated wafer was exposed to UV irradiation (λ = 365 nm, power >20 mW/cm^2) for 2 min to cure the Fluorocur resin. The elastomeric mold was then removed from the master template by gently peeling it away from the silicon surface.

In these experiments, the PRINT particles were derived from a mixture composed of 67 wt % trimethyloylpropane ethoxylate triacrylate (MW = 428 g/mol), 20 wt % poly(ethylene glycol) monomethylether monomethacrylate (MW = 1,000 g/mol), 10 wt % 2-aminoethylmethacrylate hydrochloride (AEM·HCl), 2 wt % fluorescein-*O*-acrylate, and 1 wt % 2,2-diethoxyacetophenone. A 10% (wt/vol) solution of this mixture in 2-propanol was prepared and then sprayed onto a Fluorocur patterned mold by using an air brush. A poly(ethylene) sheet (American Plastics Co.) was then placed over the mold and peeled back at a rate of ≈2.5 cm/min. After this, the mold was placed in a UV curing chamber, purged with nitrogen for 2 min, and UV irradiation applied (λ = 365 nm, power >20 mW/cm^2) for 2 min.

A physical means for harvesting the particles was used by placing a 2-ml aliquot of acetone [filtered through a 0.22-μm polytetrafluoroethylene (PTFE) filter] on the particle-filled mold. This drop of acetone was gently moved along the surface of the mold by using a glass slide, facilitating release of the particles from the mold. The suspended particles were collected in a 50-ml Falcon tube, centrifuged by using a IEC CENTRA CL2 Centrifuge (Thermo Electron Corporation), and rinsed with fresh acetone four times. The particles were then transferred to a tarred Eppendorf tube, and centrifuged in a microfuge (Fisher Scientific) for 20 min. The supernatant was removed, the pellet was dried in a vacuum oven overnight, massed, and dispersed in the appropriate amount of sterile water to make a 10 mg/ml dispersion of particles.

Particle Size Analysis of PRINT Particles by Using Scanning Electron Microscopy. The size of PRINT particles was analyzed via scanning electron microscopy (Hitachi model S-4700). Particle dispersions were prepared at concentrations of 0.5 mg/ml, and a drop of this solution was placed on a glass slide. The drop was then allowed to dry, and the glass slide was coated with 1.5 nm of Pd/Au alloy by using a Cressington 108 auto sputter coater (Cressington Scientific Instruments). The Pd/Au-coated glass slide was then adhered to the sample holder by using double-sided adhesive tape, and placed inside the vacuum chamber of the SEM and observed under low vacuum (10^{-3} Torr). (See Table S1.)

Zeta Potential Measurements. The zeta potential of PRINT particles was measured by using a ZetaPlus Zeta Potential Analyzer (Brookhaven Instruments). The particles were dispersed in water at a concentration of 0.3 mg/ml and the zeta potential was measured. (See Table S2.)

***In Vitro* Cytotoxicity.** HeLa cells were seeded in 100 μl of media [Minimum Essential Medium (MEM) containing Earle's salts and supplemented with 1 mM sodium pyruvate and nonessential amino acids] at a density of 5×10^3 cells per cm^2 into a 96-well microtiter plate. Cells were allowed to adhere for 24 h before MEM was replaced with Opti-MEM (90 μl per well) and the particle preparation (10 μl per well in PBS). HeLa cells were incubated with the PRINT particles for 4 h or 72 h at 37°C in a humidified 5% CO_2 atmosphere. After the incubation period, negative controls were prepared by the addition of 2 μl of lysis solution to a few wells containing cells only. After 2 min, the MTS assay solution was added (20 μl per well) into each well. The cells were then incubated for an additional 1 h at 37°C in a humidified 5% CO_2 atmosphere. The optical density at 492 nm was measured by using a Bio-Rad model 3550 microplate reader (Bio-Rad Laboratories). The viability of the cells exposed to PRINT particles was expressed as a percentage of the viability of cells grown in the absence of particles.

Uptake Experiments. The HeLa cell line was used to investigate the uptake of 5-μm, 3-μm, and 2-μm cubic particles and 1-μm, 0.5-μm [aspect ratio (AR) = 2], 0.2-μm (AR = 1), 0.15-μm (AR = 3), and 0.1-μm (AR = 3) cylindrical particles. Particles were incubated with cells over a time course ranging from 15 min to 4 h (37°C, 5% CO_2). After cell/particle incubation, the cells were washed and detached by trypsinization. After centrifugation, cells were resuspended in a 0.4% trypan blue (TB) solution in Dulbecco's Phosphate Buffers Saline solution (D-PBS) to quench the extracellular FITC fluorescence (20). This assay is based on the observation that the vital dye TB, while quenching the FITC fluorescence of a noninternalized particle, causes them to fluoresce red whereas an internalized particle will fluoresce green. Cells were then centrifuged, the TB solution was removed, the cell pellet was resuspended in DPBS, and sample was analyzed by flow cytometry (CyAn ADP, Dako), for green and red fluorescence. There were 10,000 cells measured in each sample.

Confocal Laser Scanning Microscopy. HeLa cells (50,000) were seeded in a T-25 flask for 24 h (37°C, 5% CO_2). Cells were washed once with D-PBS followed by MEM with supplements containing 1% FBS (low serum). Cells were then incubated for 4 h (37°C, 5% CO_2) with low serum MEM (2 ml) containing 15 μg/ml FITC-labeled PRINT particles. The cells were then washed by detachment with trypsin, resuspended in complete MEM containing 10% FBS, replated onto two 35-mm^2 glass bottom dishes with 1.5G coverslips (MatTek Corp.) and allowed to adhere overnight at 37°C. Nuclei were stained with 2.5 μM DRAQ5 (Biostatus Ltd.) in complete MEM according to the manufacturer's protocol. DRAQ5 is a DNA-specific dye with far-red fluorescent properties (Ex: 647 nm, Em: 670 nm) (31). AlexaFluor-555-labeled WGA in D-PBS (2.5 μg/ml; Molecular Probes) was used to visualize plasma membranes. Cells were then fixed with 4% paraformaldehyde. Microscopy was carried out on an Olympus FV500 confocal laser scanning microscope (Olympus) located in the Microscopy Laboratory Services, a core facility of the Department of Pathology and

Laboratory Medicine within the UNC School of Medicine. *Z* stacks were collected and used for 3D reconstruction and visualization of intracellular particle localization.

Transmission Electron Microscopy (TEM). TEM was carried out to further visualize the intracellular internalization and localization of PRINT particles. $\approx 5 \times 10^5$ HeLa cells were seeded in 60-mm^2 polystyrene dishes overnight. The following day, cells were treated with either 200 nm (AR = 1), 1 μm (AR = 1), or 150 nm (AR = 3) particles (15 μg/ml in reduced serum MEM) for times indicated in the figure legend. Cell monolayers were rinsed with D-PBS and fixed in 2% paraformaldehyde/2.5% glutaraldehyde/0.15M sodium phosphate at pH 7.4, for several hours or overnight. After three rinses with sodium phosphate buffer, the monolayers were postfixed for 1 h in 1% osmium tetroxide/1.25% potassium ferrocyanide/0.15M sodium phosphate buffer. After rinsing in deionized water, the cells were dehydrated by using increasing concentrations of ethanol (30%, 50%, 75%, 100%, 100%, 10 min each) and embedded in Polybed 812 epoxy resin (Polysciences). The monolayers were sectioned parallel and perpendicular to the substrate at 70 nm by using a diamond knife. Ultrathin sections were collected on 200-mesh copper grids and stained with 4% aqueous uranyl acetate for 15 min, followed by Reynolds' lead citrate for 7 min. Samples were viewed by using a LEO EM910 transmission electron microscope operating at 80 kV (LEO Electron Microscopy) located at the Microscopy Laboratory Services Core Facility. Digital images were acquired by using a Gatan Orius SC1000 CCD Digital Camera and Digital Micrograph 3.11.0 (Gatan, Inc.).

Inhibitor Studies. 5×10^4 HeLa cells seeded in a T-25 flask were treated with 0.1% NaN_3/50 mM 2-deoxyglucose, cytochalasin D (5 μg /ml), Dynasore (80 μM), or genistein (200 μM) in serum-free MEM for 1 h before incubation of particles (15 μg/ml) with inhibitor in the fresh media for 1 h at 37°C/5% CO_2. For the inhibitors methyl-β-cyclodextrin (mβcd) and chlorpromazine, cells were preincubated in serum-free MEM containing either in 5 mM mβcd or 10 μg/ml chlorpromazine for 15 min at 37°C/5% CO_2. The media were then changed to fresh media containing the inhibitors plus particles (15 μg/ml) and further incubated for 30 min at 37°C/5% CO_2. After exposure to particles and inhibitors for the desired time, the cells were washed with D-PBS and then trypsinized and processed for flow cytometry as described in *Uptake Experiments*. All inhibitors were obtained from Sigma-Aldrich except for Dynasore, which was obtained from ChemBridge.

ACKNOWLEDGMENTS. We thank Kevin P. Herlihy, Stuart S. Williams, and Meredith J. Hampton for the fabrication of several masters used in the current study. This work was supported in part by the STC Program of the National Science Foundation (CHE-9876674), National Institutes of Health Program Project Grant PO1-GM059299, National Institutes of Health Grant U54-CA119343 (the Carolina Center of Cancer Nanotechnology Excellence), the William R. Kenan Professorship at the University of North Carolina at Chapel Hill, and a sponsored research agreement with Liquidia Technologies.

1. Cossart P (1997) Subversion of the mammalian cell cytoskeleton by invasive bacteria. *J Clin Invest* 99:2307–2311.
2. Lukyanov AN, Elbayoumi TA, Chakilam AR, Torchilin VP (2004) Tumor-targeted liposomes: doxorubicin-loaded long-circulating liposomes modified with anti-cancer antibody. *J Controlled Release* 100:135–144.
3. Torchilin VP (2004) Targeted polymeric micelles for delivery of poorly soluble drugs. *Cell Mol Life Sci* 61:2549–2559.
4. Kabanov AV, Felgner PL, Seymour LW (1998) *Self-assembling Complexes for Gene Delivery. From Laboratory to Clinical Trial* (Wiley, Chichester).
5. Sarciaux JM, Acar L, Sado PA (1995) Using microemulsion formulations for oral-drug delivery of therapeutic peptides. *Int J Pharm* 120:127–136.
6. Duncan R, Izzo L (2005) Dendrimer biocompatibility and toxicity. *Adv Drug Delivery Rev* 57:2215–2237.
7. Barth RF, Adams DM, Soloway AH, Alam F, Darby MV (1994) Boronated starburst dendrimer monoclonal-antibody immunoconjugates—Evaluation as a potential delivery system for neutron-capture therapy. *Bioconjugate Chem* 5:58–66.
8. Bianco A, Kostarelos K, Prato M (2005) Applications of carbon nanotubes in drug delivery. *Curr Opin Chem Biol* 9:674–679.
9. Metraux GS, Mirkin CA (2005) Rapid thermal synthesis of silver nanoprisms with chemically tailorable thickness. *Adv Mater* 17:412–415.
10. Champion JA, Katare YK, Mitragotri S (2007) Particle shape: A new design parameter for micro- and nanoscale drug delivery carriers. *J Controlled Release* 121:3–9.
11. Euliss LE, DuPont JA, Gratton S, DeSimone J (2006) Imparting size, shape, and composition control of materials for nanomedicine. *Chem Soc Rev* 35:1095–1104.
12. Geng Y, *et al.* (2007) Shape effects of filaments versus spherical particles in flow and drug delivery. *Nat Nanotechnol* 2:249–255.
13. Rejman J, Oberle V, Zuhorn IS, Hoekstra D (2004) Size-dependent internalization of particles via the pathways of clathrin-and caveolae-mediated endocytosis. *Biochem J* 377:159–169.
14. Zauner W, Farrow NA, Haines AMR (2001) In vitro uptake of polystyrene microspheres: Effect of particle size, cell line and cell density. *J Controlled Release* 71:39–51.
15. Champion JA, Mitragotri S (2006) Role of target geometry in phagocytosis. *Proc Natl Acad Sci USA* 103:4930–4934.
16. Xia Y, Whitesides GM (1998) Soft lithography. *Angew Chem* 110:568–594.
17. Rolland JP, *et al.* (2005) Direct fabrication and harvesting of monodisperse, shape-specific nanobiomaterials *J Am Chem Soc* 127:10096–10100.
18. Gratton SEA, *et al.* (2007) Nanofabricated particles for engineered drug therapies: A preliminary biodistribution study of PRINT (TM) nanoparticles. *J Controlled Release* 121:10–18.
19. Rolland JP, Hagberg EC, Denison GM, Carter KR, DeSimone JM (2004) High-resolution soft lithography: Enabling materials for nanotechnologies Angew. *Chem Int Ed* 43:5796–5799.
20. Fattorossi A, Nisini R, Pizzolo JG, Damelio R (1989) New, simple flow-cytometry technique to discriminate between internalized and membrane-bound particles in phagocytosis. *Cytometry* 10:320–325.
21. Garnett MC (1999) Gene-delivery systems using cationic polymers. *Crit Rev Ther Drug Carrier Syst* 16:147–207.
22. Zauner W, Ogris M, Wagner E (1998) Polylysine-based transfection systems utilizing receptor-mediated delivery. *Adv Drug Delivery Rev* 30:97–113.
23. Miller CR, Bondurant B, McLean SD, McGovern KA, O'Brien DF (1998) Liposome-cell interactions in vitro: Effect of liposome surface charge on the binding and endocytosis of conventional and sterically stabilized liposomes. *Biochemistry* 37:12875–12883.
24. Matteoni R, Kreis TE (1987) Translocation and clustering of endosomes and lysosomes depends on microtubules. *J Cell Biol* 105:1253–1265.
25. Kaksonen M, Toret CP, Drubin DG (2006) Harnessing actin dynamics for clathrin-mediated endocytosis. *Nat Rev Mol Cell Biol* 7:404–414.
26. Macia E, *et al.* (2006) Dynasore, a cell-permeable inhibitor of dynamin. *Dev Cell* 10:839–850.
27. Simionescu N, Simionescu M, Palade GE (1975) Permeability of muscle capillaries to small heme-peptides—Evidence for existence of patent transendothelial channels. *J Cell Biol* 64:586–607.
28. Conner SD, Schmid SL (2003) Regulated portals of entry into the cell. *Nature* 422:37–44.
29. Gary DJ, Puri N, Won YY (2007) Polymer-based siRNA delivery: Perspectives on the fundamental and phenomenological distinctions from polymer-based DNA delivery. *J Controlled Release* 121:64–73.
30. Oupicky D, Konak C, Ulbrich K, Wolfert MA, Seymour LW (2000) DNA delivery systems based on complexes of DNA with synthetic polycations and their copolymers. *J Controlled Release* 65:149–171.
31. Smith PJ, *et al.* (2000) Characteristics of a novel deep red/infrared fluorescent cell-permeant DNA probe, DRAQ5, in intact human cells analyzed by flow cytometry, confocal and multiphoton microscopy. *Cytometry* 40:280–291.